Non-Linear Conjugate Gradient Magnetotelluric Inversion for 2-D Anisotropic Conductivities

Josef Pek[(1)], Fernando A. M. Santos[(2)] and Yuguo Li[(3)]

[(1)]Institute of Geophysics, Acad. Sci. Czech Rep., Prague, Czech Rep. (e-mail: jpk@ig.cas.cz)
[(2)]Center of Geophysics, Univ. Lisbon, Lisbon, Portugal
[(3)]College of Marine Geosciences, Ocean Univ. China, Qingdao, China

Abstract

We report on the state of the art in the development of a non-linear conjugate gradient (NLCG) version of the 2-D inverse algorithm for magnetotelluric (MT) data over structures with arbitrary electrical anisotropy. The algorithm is based on the Occam inverse strategy. As a direct solver, our 2-D finite volume forward modeling program for structures with arbitrary anisotropy is employed, which is also further used to effectively evaluate parametric sensitivities by employing the reciprocity principle. A standard Polak-Ribiere NLCG algorithm is then applied to minimize the inversion objective function which consists of a data misfit term and of regularization penalties applied to both the structure complexity and anisotropy throughout the model. The algorithm offers considerable savings to the computing time and memory demands due to both the reciprocity-based evaluation of the parametric sensitivities and on-line computation of products of the Jacobian and its transverse with a vector within the CG algorithm. Synthetic test inversions with a single anisotropic box anomaly are presented and used to discuss expected ambiguity issues in anisotropic structures. The 2-D anisotropic inversion is further applied to a small subset of experimental MT data from the contact area of the Southern Portuguese Zone and the Ossa Morena Zone in southern Portugal, and the results are compared with those obtained earlier by a 1-D inverse and 2-D direct trial-and-error modeling approach to the same data.

1 Introduction

Over the last decades, anisotropy of the electrical conductivity in the earth has become a valuable indicator of tectonic structures and processes, both fossil and recent. Large-scale electrical macro-anisotropy manifests a specific spatial arrangement of conducting fractions in the subsurface, a specific organization of conductors which are not distinguished as separate bodies by the diffusing electromagnetic field but rather sensed as an anisotropic bulk. Interpretations of electromagnetic induction data from a vicinity of the German Continental Deep Borehole (KTB) proved that suites of graphitized fossil shear zones or faults filled with saline fluids appear as highly electrically anisotropic domains throughout the whole upper crust of the area (e.g., Eisel and Haak, 1999; Eisel *et al.*, 2001). Crustal anisotropic structures were later modeled, and put into regional tectonic plots, in several regional MT studies, e.g., by Lezaeta and Haak (2003), Heise and Pous (2003) or by Weckmann *et al.* (2003), with special regard to the phenomenon of MT phases exceeding 90°. Brasse *et al.* (2008) could explain systematic deflections of long-period induction arrows over the South Chilean continental margin by regional 2-D anisotropy due to a deeply fractured, fluid-rich crust in the region. Deep sub-crustal electromagnetic investigations as well as attempts of interpreting jointly the seismic and electric anisotropy in the lithospheric and sub-lithospheric upper mantle have evolved into promising indicators of large-scale structures and deformation processes in the Earth (see, e.g., Mareschal *et al.*, 1995; Simpson, 2001; Bahr and Simpson, 2002; Hamilton *et al.*, 2006; Padilha *et al.*, 2006; Roux *et al.*, 2011; Ruiz-Constán *et al.*, 2012). See Wannamaker (2005) for a more thorough review on the electrical anisotropy and its relations to deep geological and tectonic processes.

The sample of the induction studies mentioned above clearly evidenced the existence of crustal and upper mantle electrical anisotropy. The studies also demonstrated that macro-anisotropic structures can be

often treated mathematically as earth sub-domains with continuous intrinsic anisotropy. This approximation simplifies the modeling of inductive responses considerably, as highly heterogeneous structures, often involving series of thin and highly conducting sheet-like bodies, can be modeled by a single large-scale anisotropic bulk.

Methods for the direct numerical modeling of MT fields in laterally inhomogeneous structures with arbitrary anisotropy have been around since the paper by Reddy and Rankin (1975) who presented the first finite element algorithm for 2-D structures with azimuthal electrical anisotropy. A finite volume algorithm for MT fields in 2-D structures with general biaxial anisotropy was published by Pek and Verner (1997), and the finite element version of the same algorithm was presented by Li (2002). The latter algorithm was later extended to allow for an automatic mesh adaptation in the direct simulations by Li and Pek (2008). A 3-D finite difference code for the modeling of MT fields in anisotropic structures was presented by Weidelt (1999), and a number of algorithms exist for the simulation of controlled source electromagnetic fields in 3-D generally anisotropic media (e.g., Wang and Fang, 2001; Weiss and Newman, 2002; Davydycheva *et al.*, 2003; Hou *et al.*, 2006; Zaslavsky *et al.*, 2011).

As it can be often difficult to even qualitatively suggest particular anisotropic structures that can account for specific features in the experimental MT data, inverse MT solutions for anisotropic conductivities in the earth are highly desirable. Although a few inverse algorithms for anisotropic conductivities have been presented for geoelectric and electromagnetic applications with controlled source (Pain *et al.*, 2003; Ramananjaona and MacGregor, 2010), they cannot be immediately applied to the MT case because of largely different sensitivity patterns of anisotropic media for different source types and geometries. For MT inversions for laterally non-uniform anisotropic media, two approaches have been presented so far: a 2-D inversion for a conductivity tensor aligned with the model coordinate frame by Mackie (based on the 2-D inverse code by Rodi and Mackie, 2001) and an inverse algorithm by Li *et al.* (2003) for a general conductivity tensor in the 2-D model. The latter algorithm was an attempt for a complete solution to the 2-D anisotropic MT inverse problem. The solution was based on a damped Gauss-Newton minimization of a penalized objective function and made it possible to employ non-quadratic structure and anisotropy penalties to regularize the inverse solution. Due to stability problems with practical MT data, development of the algorithm has been discontinued, but substantial portions of the work spent on that method have been included into the present version of the non-linear conjugate gradient inverse procedure.

As compared to the 2-D isotropic case, the inversion for anisotropic conductivities has to cope with increased number of parameters (by a factor of 6 for the most general anisotropy case, and by a factor of 3 in the most common case of anisotropy due to a finely laminated structure), with a more complex direct solution and sensitivity computations (coupled partial differential equations for coupled field modes in the anisotropic case), and also with a largely more complex pattern of equivalencies and ambiguities of the anisotropy parameters.

This paper reports on the current development of a non-linear conjugate gradient (NLCG) version of the 2-D inverse algorithm for magnetotelluric (MT) data over structures with arbitrary electrical anisotropy. The structure of the paper is as follows: In the following section, we present a brief description of the NLCG algorithm along with the pre-requisites necessary for its application to the anisotropic 2-D MT inversion. In Section 3, we present two simple synthetic tests of the inverse algorithm and discuss ambiguity issues in 2-D anisotropic models. Finally, in Section 4, we compare results of the anisotropic inversion applied to a small subset of practical MT data from a contact area of the Southern Portuguese Zone and the Ossa Morena Zone, southern Portugal, with those obtained for the same data set earlier by a 1-D inversion and a trial-and-error 2-D direct modeling. Section 5, Conclusion, summarizes the main results achieved.

2 NLCG Inversion Algorithm

2.1 2-D Magnetotelluric Model with Arbitrary Anisotropy

Here, we adopt the 2-D MT model with arbitrary anisotropy exactly in the form as it was introduced in (Pek and Verner, 1997). A 2-D conducting medium (earth) occupies the half-space $z > 0$ and its (structural) strike is parallel to the x-coordinate axis. The conductor is generally characterized by a symmetric, positive definite 3×3 conductivity tensor $\boldsymbol{\sigma}(\mathbf{r})$, where $\mathbf{r}$ is a position vector, $\mathbf{r} = (x, y, z)$.

Locally, i.e. in each point of the medium, an orthonormal transformation exists that diagonalizes the conductivity tensor. This transformation can be expressed through three rotations around the coordinate axes (Euler rotations), and the conductivity tensor can be generally written in the form

$$\boldsymbol{\sigma} = \mathbf{R}_z(-\alpha_S)\,\mathbf{R}_x(-\alpha_D)\,\mathbf{R}_z(-\alpha_L)\ \mathrm{diag}\{\sigma_1,\sigma_2,\sigma_3\}\,\mathbf{R}_z(\alpha_L)\,\mathbf{R}_x(\alpha_D)\,\mathbf{R}_z(\alpha_S), \tag{1}$$

where σ_1, σ_2, σ_3 are the principal conductivities, and α_S, α_D, α_L are the anisotropy strike, dip and slant, respectively. Matrix $\mathbf{R}_\xi(\alpha)$ symbolizes a rotation around the current axis ξ through the angle α. Eq. (1) is true in each point $\mathbf{r}$ of the conductor but is generally spatially dependent. The position argument $\mathbf{r}$ is omitted for brevity here and in what follows. The air layer, $z < 0$, is assumed to be filled with an ideal insulator ($\sigma_{\mathrm{air}} = 0$).

Magnetotelluric field in the model is excited by a uniform, time-harmonic plane wave originating from sources at $z \to -\infty$. We assume the time-harmonic factor of the form $\exp(-i\omega t)$ here, where $\omega = 2\pi/T$ is the angular frequency corresponding to the period T and t is time.

With the MT model described above, Maxwell's equations in the diffusive approximation reduce to a coupled pair of partial differential equations of the second order for the strike-parallel field components, E_x and H_x, of the form (Pek and Verner, 1997)

$$\frac{\partial^2 E_x}{\partial y^2} + \frac{\partial^2 E_x}{\partial z^2} + i\omega\mu_0(\sigma_{xx} + \sigma_{xy}L + \sigma_{xz}K)E_x + i\omega\mu_0 A\frac{\partial H_x}{\partial y} - i\omega\mu_0 B\frac{\partial H_x}{\partial z} = 0, \tag{2a}$$

$$\begin{aligned}\frac{\partial}{\partial y}\left(\frac{\sigma_{yy}}{D}\frac{\partial H_x}{\partial y}\right) + \frac{\partial}{\partial z}\left(\frac{\sigma_{zz}}{D}\frac{\partial H_x}{\partial z}\right) + \frac{\partial}{\partial y}\left(\frac{\sigma_{zy}}{D}\frac{\partial H_x}{\partial z}\right) + \frac{\partial}{\partial z}\left(\frac{\sigma_{yz}}{D}\frac{\partial H_x}{\partial y}\right) + \\ + i\omega\mu_0 H_x - \frac{\partial}{\partial y}(KE_x) + \frac{\partial}{\partial z}(LE_x) = 0,\end{aligned} \tag{2b}$$

where the material coefficients A, B and K, L are given by

$$A = (\sigma_{xy}\sigma_{yz} - \sigma_{xz}\sigma_{yy})/D, \quad B = (\sigma_{xz}\sigma_{zy} - \sigma_{xy}\sigma_{zz})/D,$$

$$L = (\sigma_{yz}\sigma_{zx} - \sigma_{yx}\sigma_{zz})/D, \quad K = (\sigma_{yx}\sigma_{zy} - \sigma_{yy}\sigma_{zx})/D,$$

and D is a sub-determinant of the conductivity tensor, $D = \sigma_{yy}\sigma_{zz} - \sigma_{yz}\sigma_{zy}$. In virtue of the symmetry of the conductivity tensor, we have $A = L$ and $B = K$. After solving eqs. (2), with corresponding boundary conditions, for E_x and H_x, we can obtain the complete MT field in the model by calculating the transversal field components via

$$H_y = \frac{1}{i\omega\mu_0}\frac{\partial H_x}{\partial z}, \quad H_z = -\frac{1}{i\omega\mu_0}\frac{\partial H_x}{\partial y}, \tag{3a}$$

$$E_y = \frac{\sigma_{yz}}{D}\frac{\partial H_x}{\partial y} + \frac{\sigma_{zz}}{D}\frac{\partial H_x}{\partial z} + BE_x, \quad E_z = -\frac{\sigma_{yy}}{D}\frac{\partial H_x}{\partial y} - \frac{\sigma_{yz}}{D}\frac{\partial H_x}{\partial z} + AE_x. \tag{3b}$$

Determining basic MT functions, i.e. MT impedances and vertical geomagnetic transfer functions (induction arrows), requires us to solve the above system of equations for two independent polarizations of the exciting field. Then, if a field component F is linearly related to the horizontal magnetic components through $F = T_x H_x + T_y H_y$, we easily obtain

$$T_x = \frac{F^{(1)}H_y^{(2)} - H_y^{(1)}F^{(2)}}{H_x^{(1)}H_y^{(2)} - H_y^{(1)}H_x^{(2)}}, \quad T_x = \frac{H_x^{(1)}F^{(2)} - F^{(1)}H_x^{(2)}}{H_x^{(1)}H_y^{(2)} - H_y^{(1)}H_x^{(2)}}, \tag{4}$$

where the superscripts (1), (2) distinguish MT fields for the two polarizations.

2.2 Numerical Solution to the Direct Problem

Analytical solution to Eqs. (2) has not been given yet even for the simplest 2-D models. To solve that system numerically, a standard finite volume (FV) approximation of (2) was presented by Pek and Verner (1997). Alternatively, a finite element (FE) algorithm for the same problem was developed by Li (2002).

By discretizing the system of equations (2), with the corresponding boundary conditions, on a FV mesh we arrive at a system of linear algebraic equations, $\mathbf{A}\mathbf{x} = \mathbf{b}$, for the approximate strike-parallel fields $\mathbf{u}$. The matrix $\mathbf{A}$ is a symmetric banded complex matrix which depends on the conductivities and on the geometry of the mesh. The r.h.s. vector $\mathbf{b}$ depends on the fields on the outer boundaries of the computation domain (Dirichlet boundary conditions). Remember that $\mathbf{x}$ involves both the electric and magnetic components of the MT field because of the mode coupling in anisotropic media. Remember also that, from the point of view of the inverse problem, one direct solution represents, in fact, a number of solutions computed for a suite of periods and, at each period, for two independent polarizations,

$$\mathbf{A}\mathbf{x} = \mathbf{b} \;\Leftrightarrow\; \begin{pmatrix} \mathbf{A}(T_1) & 0 & \dots & 0 & 0 \\ 0 & \mathbf{A}(T_1) & \dots & 0 & 0 \\ \vdots & \vdots & \ddots & \vdots & \vdots \\ 0 & 0 & \dots & \mathbf{A}(T_{N_{\rm per}}) & 0 \\ 0 & 0 & \dots & 0 & \mathbf{A}(T_{N_{\rm per}}) \end{pmatrix} \begin{pmatrix} \mathbf{x}^{(1)}(T_1) \\ \mathbf{x}^{(2)}(T_1) \\ \vdots \\ \mathbf{x}^{(1)}(T_{N_{\rm per}}) \\ \mathbf{x}^{(2)}(T_{N_{\rm per}}) \end{pmatrix} = \begin{pmatrix} \mathbf{b}^{(1)}(T_1) \\ \mathbf{b}^{(2)}(T_1) \\ \vdots \\ \mathbf{b}^{(1)}(T_{N_{\rm per}}) \\ \mathbf{b}^{(2)}(T_{N_{\rm per}}) \end{pmatrix}, \tag{5}$$

where T_i, $i = 1, \dots, N_{\rm per}$ are the periods for which the solution is to be calculated.

As a 2-D MT direct problem for anisotropic media is mostly of moderate size, we use Gaussian elimination procedure to solve the systems (5). For each period of the field, the elimination step is carried out in full for one polarization only and the eliminated form of the matrix $\mathbf{A}(T_i)$ is stored. This can be later used to carry out a fast elimination step for only the r.h.s. vector $\mathbf{b}^{(2)}(T_i)$ in the second polarization, without the necessity of repeating the time consuming complete elimination procedure for $\mathbf{A}(T_i)$ once again. The fast back-substitution step is identical for both polarizations. After the approximate solution $\mathbf{u}(T_i)$ has been found, transversal fields (3) are computed by using a spatial derivative procedure by Weaver *et al.* (1985, 1986) generalized to anisotropic models (see Pek *et al.*, 2003). From the solutions for both field polarizations, required MT functions are obtained easily from (4).

2.3 Computation of Parametric Sensitivities

Sensitivities of the MT fields and functions are essential parts of inverse algorithms as they allow us to find parametric changes in the model required to improve the fit between the model and observed data. Sensitivities with respect to the parameters of a 2-D anisotropic model can be evaluated by differentiating the field components or MT functions with respect to the model parameters, i.e. with respect to σ_j (or $\varrho_j = \sigma_j^{-1}$), $j = 1, 2, 3$, and α_S, α_D, α_L, eq. (1), for each specified homogeneous domain of the model. Following the ideas by Rodi (1976), Jupp and Vozoff (1977), Červ and Pek (1981) and Rodi and Mackie (2001), Pek *et al.* (2003) developed a numerical algorithm for the parametric sensitivities in 2-D MT models with arbitrary anisotropy. Starting from (5), approximate parametric sensitivities of the strike-parallel field components with respect to an arbitrary parameter p are given by

$$\frac{\partial \mathbf{x}}{\partial p} = -\,\mathbf{A}^{-1}\left(\frac{\partial \mathbf{A}}{\partial p}\,\mathbf{x} + \frac{\partial \mathbf{b}}{\partial p}\right) \equiv -\,\mathbf{A}^{-1}\mathbf{r}_p, \tag{6}$$

where $\mathbf{r}_p$ is a vector which depends on conductivities, mesh geometry, boundary conditions, as well as on the direct solution $\mathbf{x}$. Vector $\mathbf{r}_p$ is parameter (p) dependent. Since (6) is a pseudo-direct problem (i.e., it has the same matrix $\mathbf{A}$ as the direct solution, but the r.h.s. is different), we can solve it fast by making use of the eliminated form of the matrix $\mathbf{A}$ which had been stored earlier. Eq. (6) has to be solved once for each parameter p for which the sensitivity is needed.

Even more speedup in the sensitivity calculations can be achieved if reciprocity principle is applied (Rodi and Mackie, 2001; Pek *et al.*, 2003). If (6) is solved directly we obtain the parametric sensitivity with respect to p in all mesh nodes throughout the model, which mostly represents a lot of redundant information. If the sensitivities are needed for only a single index (mesh node), say δ, we can pick out that index by multiplying the complete sensitivity $\partial\mathbf{x}/\partial p$ by a vector $\mathbf{\Delta}_\delta$ which consists of zeros everywhere except at the δ-th position where it is one,

$$\frac{\partial x_\delta}{\partial p} = \mathbf{\Delta}_\delta^T\,\frac{\partial \mathbf{x}}{\partial p} = \underline{-\,\mathbf{\Delta}_\delta^T\,\mathbf{A}^{-1}\mathbf{r}_p = -\,\mathbf{\Delta}_\delta^T\,(\mathbf{A}^T)^{-1}\mathbf{r}_p} = -\,(\mathbf{A}^{-1}\mathbf{\Delta}_\delta)^T\mathbf{r}_p. \tag{7}$$

The underlined part of the formula shows where the symmetry of the normal matrix is used, $\mathbf{A} = \mathbf{A}^T$, which is a manifestation of the physical reciprocity principle in the numerical domain. By employing (7),

we obtain sensitivities with respect to *all parameters* at a single mesh node for the price of only one single pseudo-forward solution $\mathbf{q}_\delta = \mathbf{A}^{-1}\mathbf{\Delta}_\delta$. This must be solved repeatedly if the sensitivities in several nodes, with different 'pickers' $\mathbf{\Delta}$, are required. The idea of eq. (7) can be easily extended to more general 'picker' vectors which may span several mesh nodes and even depend on the model parameters. In this way, the reciprocity computations can be employed immediately to numerically evaluate parametric sensitivities of the transversal MT fields (3) and MT functions (4).

Formulas for the transversal fields (3), when numerically approximated, lead to linear interpolation filters in an, at most, 9-point vicinity of the central mesh node δ, $F_\delta = \mathbf{P}_\delta^T(\mathbf{p})\,\mathbf{x}$, for any transversal field component F (Pek *et al.*, 2003). Components of the picker vector $\mathbf{P}_\delta(\mathbf{p})$ now generally depend on the model parameters $\mathbf{p}$, but they are equal for both polarizations of the exciting field. In virtue of (7), the sensitivities of F_δ with respect to p can be computed via

$$\frac{\partial F_\delta}{\partial p} = \frac{\partial \mathbf{P}_\delta^T}{\partial p}\,\mathbf{x} + \mathbf{P}_\delta^T\,\frac{\partial \mathbf{x}}{\partial p} = \frac{\partial \mathbf{P}_\delta^T}{\partial p}\,\mathbf{x} - \mathbf{P}_\delta^T\,\mathbf{A}^{-1}\mathbf{r}_p = \frac{\partial \mathbf{P}_\delta^T}{\partial p}\,\mathbf{x} - (\mathbf{A}^{-1}\mathbf{P}_\delta)^T\mathbf{r}_p\,. \tag{8}$$

Evaluating the first term on the r.h.s. of (8) is elementary. The second term requires one pseudo-forward solution, $\mathbf{q}_\delta = \mathbf{A}^{-1}\mathbf{P}_\delta$, for each field component for which the sensitivities are needed. Once $\mathbf{q}_\delta$ is found, evaluating any sensitivity for F_δ is a matter of a simple multiplication of $\mathbf{q}_\delta^T$ with the respective vector $\mathbf{r}_p$.

Parametric sensitivities of the MT transfer functions (4) can be computed either by using (7), (8) in formulas (4) which have been differentiated directly with respect to p, or by deriving corresponding picker vectors $\mathbf{P}_{T\delta}$ for the MT functions considered. In the latter approach, we write the MT functions (4) in a general functional form, $T_\delta = f(F_{i\delta})$, where $F_{i\delta}$, $i = 1, \ldots$, symbolize field components at the δ-th mesh node for any polarization. As $F_{i\delta} = \mathbf{P}_{i\delta}^T\,\mathbf{x}$ according to what was said in the previous paragraph, we can write for the parametric sensitivities of T,

$$\begin{aligned}
\frac{\partial T_\delta}{\partial p} &= \sum_i \frac{\partial T_\delta}{\partial F_{i\delta}}\,\frac{\partial F_{i\delta}}{\partial p} = \sum_i \frac{\partial T_\delta}{\partial F_{i\delta}}\left(\frac{\partial \mathbf{P}_{i\delta}^T}{\partial p}\,\mathbf{x} - \mathbf{P}_{i\delta}^T\,\mathbf{A}^{-1}\mathbf{r}_p\right) = \\
&= \left(\sum_i \frac{\partial T_\delta}{\partial F_{i\delta}}\,\frac{\partial \mathbf{P}_{i\delta}^T}{\partial p}\right)\mathbf{x} - \left(\sum_i \frac{\partial T_\delta}{\partial F_{i\delta}}\,\mathbf{P}_{i\delta}^T\right)\mathbf{A}^{-1}\mathbf{r}_p = \left(\sum_i \frac{\partial T_\delta}{\partial F_{i\delta}}\,\frac{\partial \mathbf{P}_{i\delta}^T}{\partial p}\right)\mathbf{x} - \left(\mathbf{A}^{-1}\sum_i \frac{\partial T_\delta}{\partial F_{i\delta}}\,\mathbf{P}_{i\delta}\right)^T\mathbf{r}_p \equiv \\
&\equiv \mathbf{w}_x^T\mathbf{x} - (\mathbf{A}^{-1}\mathbf{w}_p)^T\mathbf{r}_p.
\end{aligned} \tag{9}$$

Formally, eq. (9) looks the same as (8), only with more complex coefficients. Again, we need to solve only one pseudo-forward problem to evaluate all sensitivities of the function T at the node δ.

2.4 Inverse Problem

The MT inverse problem for 2-D generally anisotropic conductivity in the earth is formulated as a minimization problem for a target functional

$$\Phi(\mathbf{p}|\lambda_s, \lambda_a, \mathbf{p}_{\mathrm{ref}}) = \Phi_d(\mathbf{p}) + \lambda_s\Phi_s(\mathbf{p}|\mathbf{p}_{\mathrm{ref}}) + \lambda_a\Phi_a(\mathbf{p}|\mathbf{p}_{\mathrm{ref}}), \tag{10}$$

where Φ_d is a misfit between the model and observed data, and Φ_s, Φ_a are structure complexity and anisotropy penalties, respectively, with respective weights λ_s, λ_a. The vector $\mathbf{p}$ aggregates the model parameters, which are in our case logarithms of the principal resistivities and the anisotropy directions, i.e. strike, dip and slant, eq. (1), or any subset of those, in each homogeneous model sub-domain selected for inversion. The vector $\mathbf{p}_{\mathrm{ref}}$ contains parameters of a reference model which gives a way how to incorporate prior information into the inverse procedure. If a reference model is introduced, the minimization parameters are $\Delta\mathbf{p} = \mathbf{p} - \mathbf{p}_{\mathrm{ref}}$ instead of $\mathbf{p}$, and the inversion searches for deviations of the parameters $\mathbf{p}$ from the reference model $\mathbf{p}_{\mathrm{ref}}$ which minimize (10). In the following we omit the reference model $\mathbf{p}_{\mathrm{ref}}$ from the notations for simplicity.

The data misfit term in (10) is defined in the least-squares sense as

$$\Phi_d(\mathbf{p}) = \left\| \mathbf{C}_d^{-1}[\,\mathbf{d}^{\mathrm{obs}} - \mathbf{d}^{\mathrm{mod}}(\mathbf{p})\,]\right\|^2 = [\,\mathbf{d}^{\mathrm{obs}} - \mathbf{d}^{\mathrm{mod}}(\mathbf{p})\,]^T(\mathbf{C}_d^{-1})^T\mathbf{C}_d^{-1}[\,\mathbf{d}^{\mathrm{obs}} - \mathbf{d}^{\mathrm{mod}}(\mathbf{p})\,], \tag{11}$$

where $\mathbf{d}^{\mathrm{mod}}(\mathbf{p})$ is a vector of modeled data for parameters $\mathbf{p}$, $\mathbf{d}^{\mathrm{obs}}$ are experimental measured data, and $\mathbf{C}_d$ is a covariance matrix of the observations. As in anisotropic modeling the secondary, diagonal

elements of the MT impedance tensor are of particular importance, we use real and imaginary parts of all four components of the impedance tensor and of both components of the vertical geomagnetic transfer functions as data items in the inversion procedure.

The two regularization terms in (10) are of crucial importance for a stabilization of the MT inversion which is an ill-posed problem (e.g., Constable *et al.*, 1987; deGroot-Hedlin and Constable, 1990). The structure complexity term of (10), $\Phi_s(\mathbf{p}|\mathbf{p}_{\rm ref})$, penalizes excessive structure in the inverse model and prevents overfitting the data by structural features that are required by only the noise component in the data. We employ only simple structure penalties in the present inverse algorithm, specifically the minimum norm penalty (Tikhonov and Arsenin, 1977), and minimum roughness and minimum curvature penalties (Constable *et al.*, 1987; deGroot-Hedlin and Constable, 1990). The minimum norm functional produces the closest model with respect to the reference model, the minimum roughness and minimum curvature functionals produce smooth electrical models that still fit the data within their error bars. All these penalties can be formally written in the same form,

$$\Phi_s(\mathbf{p}|\mathbf{p}_{\rm ref}) = \| \mathbf{L}_s(\mathbf{p}-\mathbf{p}_{\rm ref}) \|^2 = (\mathbf{p}-\mathbf{p}_{\rm ref})^T \mathbf{L}_s^T \mathbf{L}_s (\mathbf{p}-\mathbf{p}_{\rm ref}), \tag{12}$$

where $\mathbf{L}_s$ is a unit matrix, or approximation to the gradient or Laplace operators for the three considered structure functionals, respectively. The matrix $\mathbf{L}_s$ is independent of the model parameters $\mathbf{p}$ in these cases. We apply the structure penalty to each of the anisotropy parameters separately, and we use one common weight λ_s for all parameters. It seems to balance well the regularization structure terms provided the logarithms of the principal resistivities and the anisotropy angles in radians are used as model parameters. It should be emphasized here that the structure penalty in the form (12) makes best sense for homogeneous model domains arranged into a rectangular grid of cells. In what follows, our model domains for the inversion will be identical with the cells of the FD grid used in the forward modeling though the inverse algorithm alone is able to operate on any disjunct set of domains within the model. A structure penalty best suited to the general case of completely irregular blocks throughout the model is the minimum norm penalty.

The aim of introducing the anisotropy penalty term, $\Phi_a(\mathbf{p})$, in the target (10) is to supress redundant anisotropy in the structure. The anisotropy penalty aims at minimizing the difference, in the least-squares sense, between the full conductivity tensor, $\boldsymbol{\sigma}$, and its mean isotropic part defined by $\bar{\boldsymbol{\sigma}}_{\rm iso} = \frac{1}{3}(\sigma_1+\sigma_2+\sigma_3)\,\mathrm{diag}\{1,1,1\}$. It can be easily shown that this leads to an anisotropy penalty form (Pain,2003)

$$\Phi_a(\mathbf{p}) = \sum_{\rm cells} (\log\varrho_1, \log\varrho_2, \log\varrho_3) \begin{pmatrix} 2 & -1 & -1 \\ -1 & 2 & -1 \\ -1 & -1 & 2 \end{pmatrix} \begin{pmatrix} \log\varrho_1 \\ \log\varrho_2 \\ \log\varrho_3 \end{pmatrix} = \\ = \sum_{\rm cells} \left[(\log\varrho_1 - \log\varrho_2)^2 + (\log\varrho_2 - \log\varrho_3)^2 + (\log\varrho_3 - \log\varrho_1)^2 \right]. \tag{13}$$

The summation in (13) runs over all anisotropic cells, or domains, of the model that are flagged for inversion. Formally, the anisotropy functional can be again expressed as $\Phi_a(\mathbf{p}) = \mathbf{p}^T \mathbf{L}_a^T \mathbf{L}_a \mathbf{p}$, similarly as the structure complexity functional (12), but with the matrix $\mathbf{L}_a$ being effective on the resistivity variables only, not on the anisotropy angles.

Eq. (1) describes the most general, biaxial conductivity anisotropy in the space. In MT practice, however, this type of anisotropy is too general, and difficult to interpret. Anisotropy in MT is most commonly understood in terms of finely layered earth domains or sub-parallel dykes which are not sensed as separate conductors by the diffusing electromagnetic field. In such cases, simpler, uniaxial anisotropy is a more useful concept in MT interpretations rather than the general case (1).

Uniaxial electrical anisotropy can be introduced as a fixed constraint by *apriori* setting, e.g., $\sigma_1 = \sigma_2$. We can easily show that, in (1), $\mathbf{R}_z(-\alpha_L)\,\mathrm{diag}\{\sigma_l,\sigma_l,\sigma_t\}\,\mathbf{R}_z(\alpha_L) = \mathrm{diag}\{\sigma_l,\sigma_l,\sigma_t\}$, where we have introduced longitudinal and transversal conductivities, $\sigma_l \equiv \sigma_1 = \sigma_2$ and $\sigma_t \equiv \sigma_3$, respectively. Thus, the slant α_L vanishes in the uniaxial case, and we can conclude that the uniaxial anisotropy is completely described by four parameters only, two principal conductivities σ_l and σ_t (or resistivities ϱ_l and ϱ_t) and two anisotropy directions, strike α_S and dip α_D. Of course, if uniaxial anisotropy is imposed as a fixed constraint we have to consider that varying σ_l implies varying both σ_1 and σ_2 simultaneously, and we must modify the sensitivities accordingly, specifically $\partial/\partial\sigma_l = \partial/\partial\sigma_1 + \partial/\partial\sigma_2$, $\partial/\partial\sigma_t = \partial/\partial\sigma_3$. In the same way, isotropy can be introduced as a fixed constraint in certain portions of the model by

setting $\sigma_{\rm iso} \equiv \sigma_1 = \sigma_2 = \sigma_3$. The parameter $\sigma_{\rm iso}$ (or, alternatively, the resistivity $\varrho_{\rm iso}$) is the only parameter that desribes the isotropic conductivity completely. A modified sensitivity must be then considered in the isotropic case, $\partial/\partial\sigma_{\rm iso} = \partial/\partial\sigma_1 + \partial/\partial\sigma_2 + \partial/\partial\sigma_3$.

Degenerate anisotropy cases, like the uniaxial anisotropy and isotropy above, can be also imposed as soft constraints on the model structure, by modifying slightly the anisotropy penalty (13) to the form

$$\Phi_a(\mathbf{p}) = \sum_{\rm cells} \left[\lambda_{a,12}(\log\varrho_1 - \log\varrho_2)^2 + \lambda_{a,23}(\log\varrho_2 - \log\varrho_3)^2 + \lambda_{a,31}(\log\varrho_3 - \log\varrho_1)^2\right]. \qquad (14)$$

If the internal weights are, e.g., $\lambda_{a,12} \gg \lambda_{a,23} = \lambda_{a,31} = 1$, the minimization of (10) will keep the principal resistivities ϱ_1 and ϱ_2 close to equal, except for those model domains where the biaxial anisotropy is highly effective at improving the fit to the data, or at decreasing the structure complexity. Soft isotropy constraint is simply imposed by increasing the overall penalty weight λ_a in (10). Incorporating the anisotropy penalty (14) in the code is straightforward while introducing the fixed constraints requires some extra decision branches to be coded for the individual degeneracy cases.

There is a number of methods that can be used to minimize the target (10) (see, e.g., Bertsekas, 1999). Here, we use the non-linear conjugate gradient (NLCG) minimization procedure that has been a core of well-known MT inversion codes by Newman and Alumbaugh (1999) and Rodi and Mackie (2001). NLCG is a class of extensions of the linear conjugate gradient method to nonquadratic problems (e.g., Andrei, 2008). NLCG algorithms are well suited for large-scale problems due to the simplicity of their iteration and their very low memory requirements. NLCG algorithms show stable and robust convergence and do not usually fail in case of ill-posed problems, where the speed of convergence is negatively affected, however. Just as in the linear case, preconditioning can improve the convergence rate of conjugate gradients.

Without going into further theoretical details, we present the NLCG version we use in our inversion algorithm as a flowchart in Fig. 1. It is Polak-Ribière form of the NLCG procedure adopted from (Rodi and Mackie, 2001), with a direct line search employed. Minimization of the target (10) starts from an initial model p_0 in the direction of the steepest descent defined by the negative of the target gradient,

$$\mathbf{g}(\mathbf{p}|\lambda_s,\lambda_a) = -2\,\mathbf{S}^T(\mathbf{p})\,(\mathbf{C}_d^{-1})^T(\mathbf{C}_d^{-1})[\,\mathbf{d}^{\rm obs} - \mathbf{d}^{\rm mod}(\mathbf{p})] + 2\,\lambda_s\mathbf{L}_s^T\mathbf{L}_s\mathbf{p} + 2\,\lambda_a\mathbf{L}_a^T\mathbf{L}_a\mathbf{p} \text{ for } \mathbf{p} = \mathbf{p}_0, \qquad (15)$$

where $\mathbf{S}(\mathbf{p})$ is a sensitivity matrix with entries $s_{ij}(\mathbf{p}) = \partial d_i^{\rm mod}(\mathbf{p})/\partial p_j$, $i = 1,\ldots,N_{\rm dat}$, $j = 1,\ldots,N_{\rm par}$. Here, $N_{\rm dat}$ and $N_{\rm par}$ are the number of measured data items and number of model parameters flagged for inversion, respectively. Subsequent steps are carried out in conjugate gradient directions which prevents the algorithm from proceeding in slow, zigzagging steps on the slope characteristic of a pure steepest descent minimization.

An essential ingredient of the NLCG iteration step is an 1-D line search for a minimum in the conjugate gradient direction. Since the direct MT problem for 2-D anisotropic conductivities is substantially faster than the evaluation of the target gradient (15), we employ a simple golden search rule (Press *et al.*, 1986) to carry out the line search. Typical number of the line search steps is between 20 and 30 in our procedure. If the target does not decrease in the line search because of loss of conjugacy due to numerical errors the NLCG process is restarted in the steepest descent direction. If the target gradient reaches a pre-defined threshold, or if the number of iterations exceeds a user defined limit, the iteration process is terminated.

As mentioned in the previous paragraph, evaluation of the target gradient (15) is the most computer resource demanding step in the minimization procedure. Substantial time savings could be already achieved by employing the reciprocity principle in the sensitivity calculations, see eqs. (7), (8), (9). The NLCG procedure gives a possibility of saving even more time and memory at computing the gradient of the data misfit in (15) (Rodi and Mackie, 2001). This part of the target gradient requires us to compute a matrix-vector product $\mathbf{S}^T(\mathbf{p})\,(\mathbf{C}_d^{-1})^T(\mathbf{C}_d^{-1})[\,\mathbf{d}^{\rm obs} - \mathbf{d}^{\rm mod}(\mathbf{p})] \equiv \mathbf{S}^T\mathbf{v}$, where $\mathbf{v}$ is a vector of model vs. data residuals normalized by the data covariance matrix. The i-th component of this product is

$$(\mathbf{S}^T\mathbf{v})_i = \sum_{j=1}^{N_{\rm dat}} \frac{\partial d_j^{\rm mod}(\mathbf{p})}{\partial p_i}\, v_j = \sum_{j=1}^{N_{\rm dat}} \left[\,\mathbf{w}_{xj}^T\,\mathbf{x} - (\mathbf{A}^{-1}\mathbf{w}_{pj})^T\mathbf{r}_{p_i}\,\right] v_j =$$

$$= \left(\sum_{j=1}^{N_{\rm dat}} v_j\mathbf{w}_{xj}\right)^T \mathbf{x} - \left(\mathbf{A}^{-1}\sum_{j=1}^{N_{\rm dat}} v_j\mathbf{w}_{pj}\right)^T \mathbf{r}_{p_i} \equiv \mathbf{W}_{xi}^T\,\mathbf{x} + (\mathbf{A}^{-1}\mathbf{W}_p)^T\mathbf{r}_{p_i}\,, \qquad (16)$$

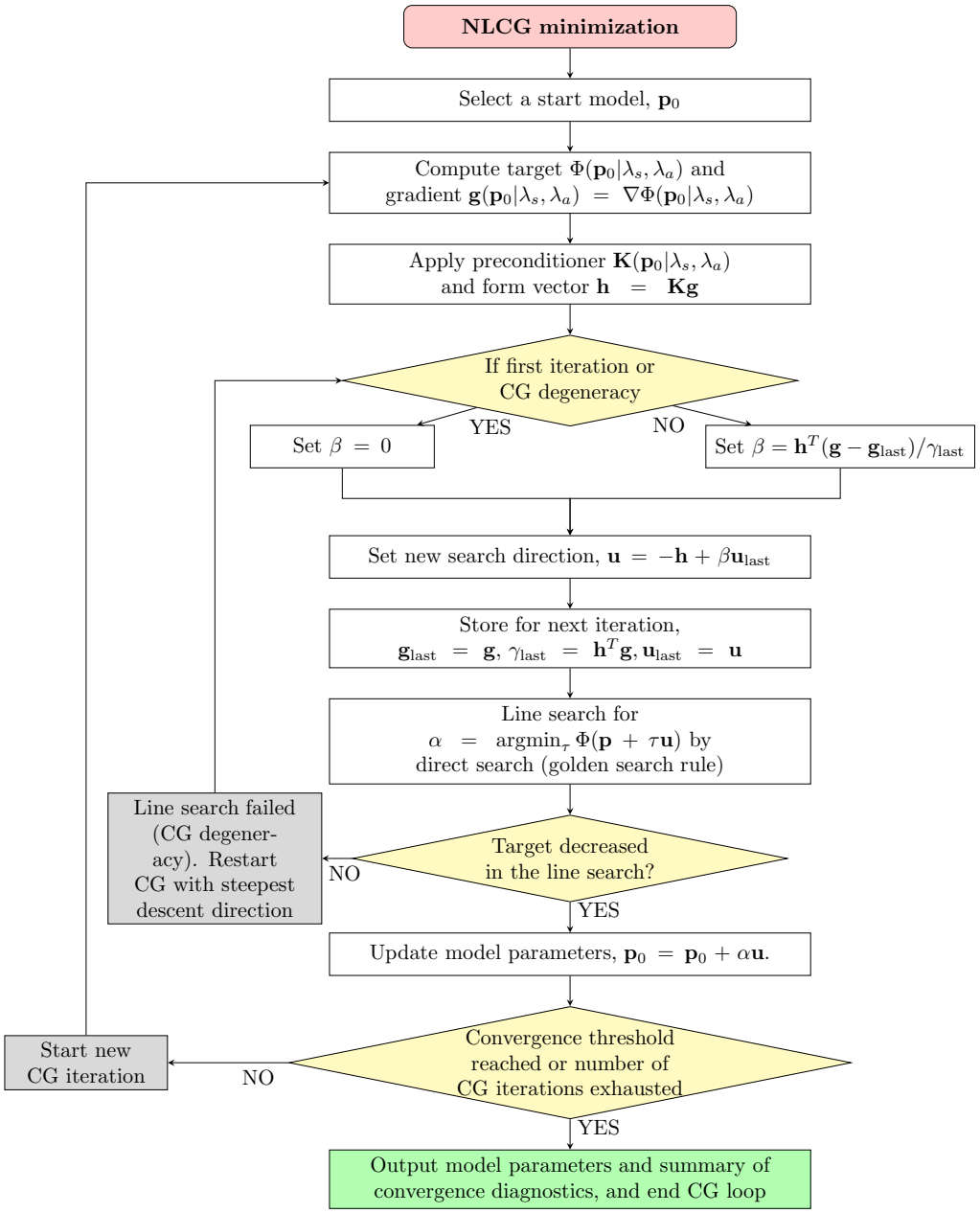

Figure 1: Flowchart of the NLCG minimization algorithm as applied to the MT inversion for 2-D anisotropic conductivities.

where eq. (9) has been used to express the sensitivities of $d_j^{\text{mod}}(\mathbf{p})$ (MT model responses) with respect to the parameter p_i. Since the vectors $\mathbf{w}_{pj}$, $j = 1,\ldots,N_{\text{dat}}$, are characteristics of the MT function $d_j^{\text{mod}}(\mathbf{p})$ only, and not of the particular p_i, we can evaluate them in the course of the forward problem solution and accumulate them, with weights v_j (data residuals), into the sum $\sum_{j=1}^{N_{\text{dat}}} v_j\mathbf{w}_{pj} = \mathbf{W}_p$. Only one pseudo-forward solution is then needed, $\mathbf{A}^{-1}\mathbf{W}_p$, for all the sensitivity computations. The vectors $\mathbf{W}_{xi}$, $i = 1,\ldots,N_{\text{par}}$, must be, however, computed for each p_i individually, but it is an easy operation. To summarize, eq. (16) says that computing the matrix-vector product $\mathbf{S}^T\mathbf{v}$ (i) does not need the elements of the sensitivity matrix $\mathbf{S}$ to be evaluated explicitly and stored, and, (ii) requires only one pseudo-forward

solution, and then, for each parameter p_i, $i = 1, \ldots, N_{\mathrm{par}}$, two vector-vector multiplications.

We use a simple Jacobi pre-conditioning to improve the convergence rate of the NLCG procedure (e.g., Newman and Boggs, 2004). In this case, the pre-conditioning matrix is an inverse diagonal of the approximate Hessian,

$$\mathbf{K}(\mathbf{p}|\lambda_s, \lambda_a) = \left\{\text{diagonal of } \left[\mathbf{S}^T(\mathbf{p})(\mathbf{C}_d^{-1})^T(\mathbf{C}_d^{-1})\mathbf{S}(\mathbf{p}) + \lambda_s \mathbf{L}_s^T\mathbf{L}_s + \lambda_a \mathbf{L}_a^T\mathbf{L}_a\right]\right\}^{-1}. \tag{17}$$

In our runs, we found that applying the pre-conditioning improved the convergence of the NLCG minimization and prevented the iterations to terminate prematurely due too small target gradients. Unfortunately, we must evaluate the individual sensitivities explicitly (though not to store them) to use the pre-conditioner (17), which does not allow us to fully exhaust the time-saving advantage implied by eq. (16) above. Therefore, we do not compute the pre-conditioner (17) in each iteration step, but update it only after a couple of iterations, typically after 5 to 10 steps in our algorithm. Fig. 2 shows the effect of the pre-conditioning for an inverse run by comparing convergence curves for both non-pre-conditioned and pre-conditioned NLCG with various update rates. The convergence is monitored as a function of iterations and of the computation time.

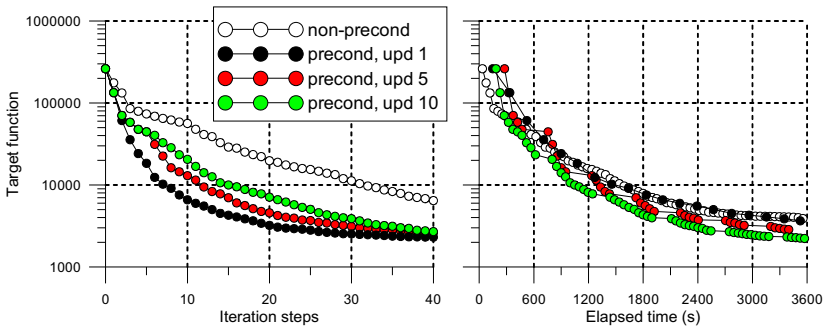

Figure 2: Effect of pre-conditioning on the NLCG iteration process. Pre-conditioned process is shown for several update rates of the pre-conditioner, specifically for updates at each iteration (upd 1), after every 5th (upd 5) and after every 10th iteration (upd 10). Left plot monitors the convergence as a function of the iteration number, right plot as a function of the computation time. The reference PC workstation was based on an Intel Core i7-940 processor and was equipped with 6 GB of RAM. Intel Visual Fortran v. 11 compiler was used to compile the code.

3 Synthetic tests

3.1 Simple 2-D Anisotropic Box Anomaly in a Uniform Host

3.1.1 Anomaly with Uniaxial Anisotropy and Anisotropy Strike only

We carried out a series of synthetic tests of the inverse MT procedure for 2-D structures with arbitrary anisotropy with very simple models in order to assess the performance of the code, as well as to indicate basic ambiguity patterns in 2-D anisotropic structures. A first test was run with synthetic data generated by a simple block anomaly, size 10×10 km^2, embedded in a uniform host half-space. The top of the anomaly is situated 2 km beneath the surface. Geometry of this test model has been adopted from (Rodi and Mackie, 2001). The host medium is isotropic, with resistivity $\varrho_{\mathrm{host}} = 300$ Ωm. The anomalous block is characterized by uniaxial anisotropy, with principal resistivities $\varrho_1 = \varrho_3 = 10$ Ωm and $\varrho_2 = 100$ Ωm and with anisotropy strike $\alpha_S = 30°$. No dip or slant are considered. Physically, the anomaly may be interpreted as a lamelar structure, with parallel vertical conducting lamelas deflected by 30° with respect to the structural strike of the model. Experimental data are simulated at seven equispaced sites above the anomalous body for 10 logarithmically equidistant periods from the range of 0.01 to 300 s. We add Gaussian noise to the data, with zero mean and a standard deviation equal to 2.5% of the maximum

module from all four impedance elements. An absolute standard deviation of 0.01 is used to add noise to geomagnetic transfer functions (induction arrows). The size of the inverse problem was: 1350 model cells, 5400 model parameters, 560 data items.

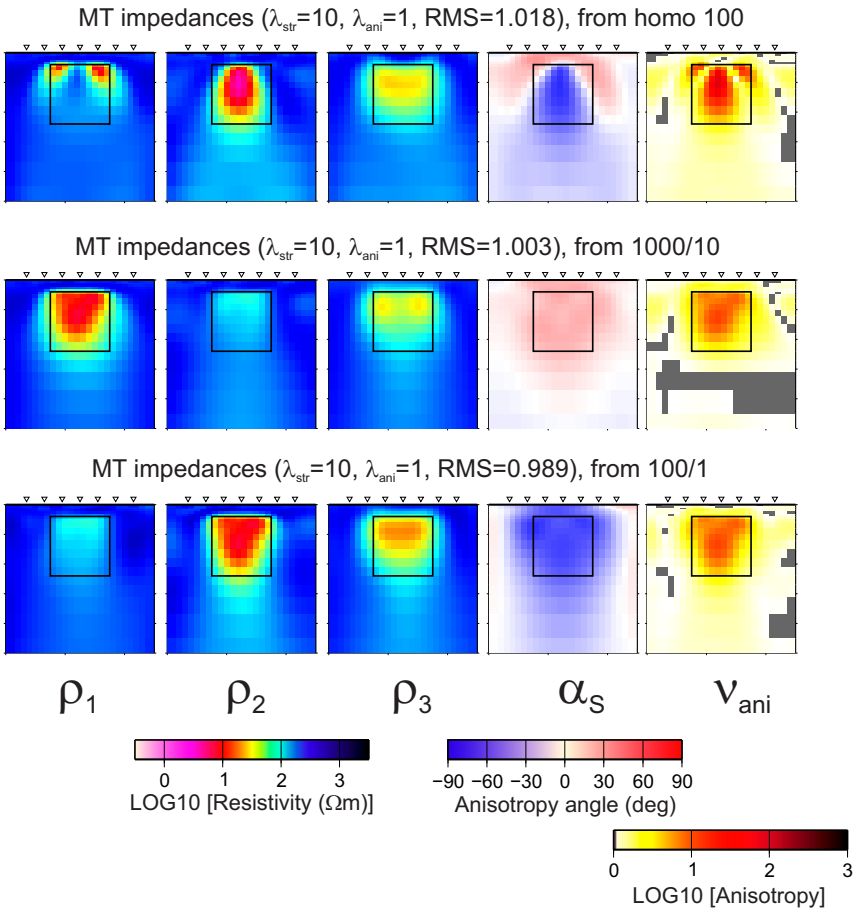

Figure 3: Three patterns of inverse models from simulated MT data for a box anomaly with uniaxial anisotropy and anisotropy strike. The models were obtained from different initial models but with the same regularization weights, $\lambda_s = 10$ and $\lambda_a = 1$. The black square shows the position of the anisotropic anomalous body. The triangles on the surface indicate observation sites. The size of the model section displayed is 25×25 km^2. The panels show, from the left to the right, the three principal resistivities, ϱ_1, ϱ_2, ϱ_3, from the inversion, the anisotropy strike α_S, and the anisotropy ratio defined as $\nu_{\text{ani}} = \varrho_{\max}/\varrho_{\min}$, where $\varrho_{\min}$, $\varrho_{\max}$ are, respectively, the minimum and maximum principal resistivities in model cells. The gray zones in the anisotropy plots indicate model domains with small anisotropy, $\varrho_{\max}/\varrho_{\min} < 1.1$. The RMS indicated for each model is computed by RMS $= \sqrt{\Phi_d(\mathbf{p})/N_{\text{dat}}}$.

In 1-D case, this type of structure is the most general anisotropic structure that can be restored from MT data, with the exception of the vertical resistivity, ϱ_3, which is principally indistinguishable in layered media (Pek and Santos, 2006). In 2-D, the vertical resistivity does affect the MT curves, but simulation studies have shown that its effect is concentrated immediately above the anomalous box and is very weak as compared to the effect of the horizontal resistivities. Thus, we can expect only very poor resolution of the 2-D inversion with respect to the vertical resistivity.

In fact, inverse runs applied to the simulated data typically show three patterns of resulting models, displayed in Fig. 3. The first pattern shows heterogeneous anisotropy within the anomaly, with $\varrho_{\max} = \varrho_1 > \varrho_2$, strike $\alpha_S = 30°$, in the top corners of the anomalous body, and $\varrho_{\max} = \varrho_2 > \varrho_1$, strike $\alpha_S = -60°$, in the body central zone. Both those zones reproduce the horizontal anisotropy correctly, but the

transition between them inside the body evidently represents an excessive structure. Though it seems to be an effect of underregularization of the model, the pattern is pervasive enough and is likely to be connected with a deep local minimum in the parameter space. The other two patterns are as expected, with only the min/max resistivites swapped. The vertical resistivity is not recovered correctly in any of the models, and is evidently result of an interplay of the starting model and of the regularization.

Figure 4 shows a complete suite of inverse results for our test model with various regularization weights, $\lambda_s \in \{1, 10, 100, 1000\}$ and $\lambda_a \in \{0, 1, 10, 100\}$. To avoid visually disturbing jumps between different quasi-equivalent model types (see Fig. 3), we started all inversion runs from the same oversmoothed model obtained from a uniform host, $\varrho_0 = 100$ Ωm, with $\lambda_s = 1000$, $\lambda_a = 10$. For small penalties, we evidently obtain models with excessive granularity and anisotropy. For strong anisotropy penalization, the recovered conductive domain becomes thinner and concentarted along the top edge of the true anomaly. The horizontal anisotropy is best recovered with the weights λ_s, λ_a close to 10 and 1, respectively. This agrees with the positions of the corresponding solutions on the L-surface (Fig. 5, left), which was suggested earlier for estimating the optimum regularization weights in 1-D anisotropic inversions (Pek and Santos, 2006).

3.1.2 Anomaly with Uniaxial Anisotropy and Anisotropy Strike and Dip

Anisotropy dip is known to be an unresolvable parameter in the 1-D anisotropic MT model unless additional information on the principal resistivites is available. A layer with the longitudinal and transversal resistivities ϱ_l and ϱ_t, respectively, and anisotropy dip α_D is sensed by MT soundings as an azimuthally anisotropic layer (i.e., with $\alpha_D = 0°$) with the horizontal resistivity (e.g., Pek and Santos, 2002)

$$\varrho_d = \varrho_l \cos^2 \alpha_D + \varrho_t \sin^2 \alpha_D. \tag{18}$$

Even for a known dip α_D, the principal resistivities ϱ_l, ϱ_t cannot be found uniquely unless one of the principal resistivities or the anisotropy ratio is known. The bottom left panel in Fig. 6 shows $\varrho_y - \varrho_z$ (transversal vs. longitudinal) equivalency lines for various dips α_D for a 1-D anisotropy model with true $\varrho_y = 100$ Ωm, $\varrho_z = 10$ Ωm, and $\alpha_D = 60°$. Any resistivity pair on any of the α_D-labeled curves produces the same horizontal resistivity ϱ_d, and is thus indistinguishable from MT data in the 1-D case.

In a 2-D case, the above equivalency is not theoretically justified, though the models equivalent in the 1-D case produce very similar MT curves also in 2-D. In Fig. 6, a few curves are demonstrated for a square 2-D anomalous body with various dipping anisotropies which would be completely equivalent in 1-D case. For the period of 30 s, the 2-D MT curves are between 20 and 30 Ωm in resistivities and between 120 and 125° in phases immediately above the anomalous body. These differences are very small, in spite of the largely different generating models. Therefore, a poor resolution of the dip by a 2-D anisotropic inversion can be expected.

One more feature of dipping anisotropy in laterally non-uniform structures should be mentioned, namely a slight asymmetry of the MT curves above the anomaly with anisotropy dip. This feature does not appear in 1-D media. Because of poor resolution with respect to the dip, this asymmetry often translates into an asymmetry of the conductivity distribution within the earth. This is clearly demonstrated in Figs. 7a and b where inversion results are shown for synthetic data from the box model in Fig. 6. In Fig. 7a, the data were inverted only for principal resistivities and anisotropy strike, the dip was fixed at $\alpha_D = 0°$. The data were fit successfully, but the recovered anisotropic conductor is shifted considerably towards the right-hand side margin of the true anomaly. Fig. 7b results from the inversion for both the principal resistivities, anisotropy strike as well as dip. A forced lamelarity of the anisotropy is demonstrated in Fig. 7c by increasing the internal anisotropy penalty weight $\lambda_{a,12}$ from 1 to 100 in (14).

Effect of extending the inverted data set by vertical geomagnetic transfer functions (induction arrows, tippers) is demonstrated in Fig. 7d. The geomagnetic data do not improve the inversion considerably as compared to Fig. 7b, they perhaps focus and centre the recovered anomaly marginally better. An attempt of employing the geomagnetic data as a source of directional information in the anisotropic inversion failed completely. Fig. 7e shows results of the inversion of the main, off-diagonal impedances jointly with the geomagnetic transfer functions, with diagonal impedances omitted. The anisotropy was not recognized properly by those data, and neither the principal resistivities nor the characteristic anisotropy directions were recovered satisfactorily.

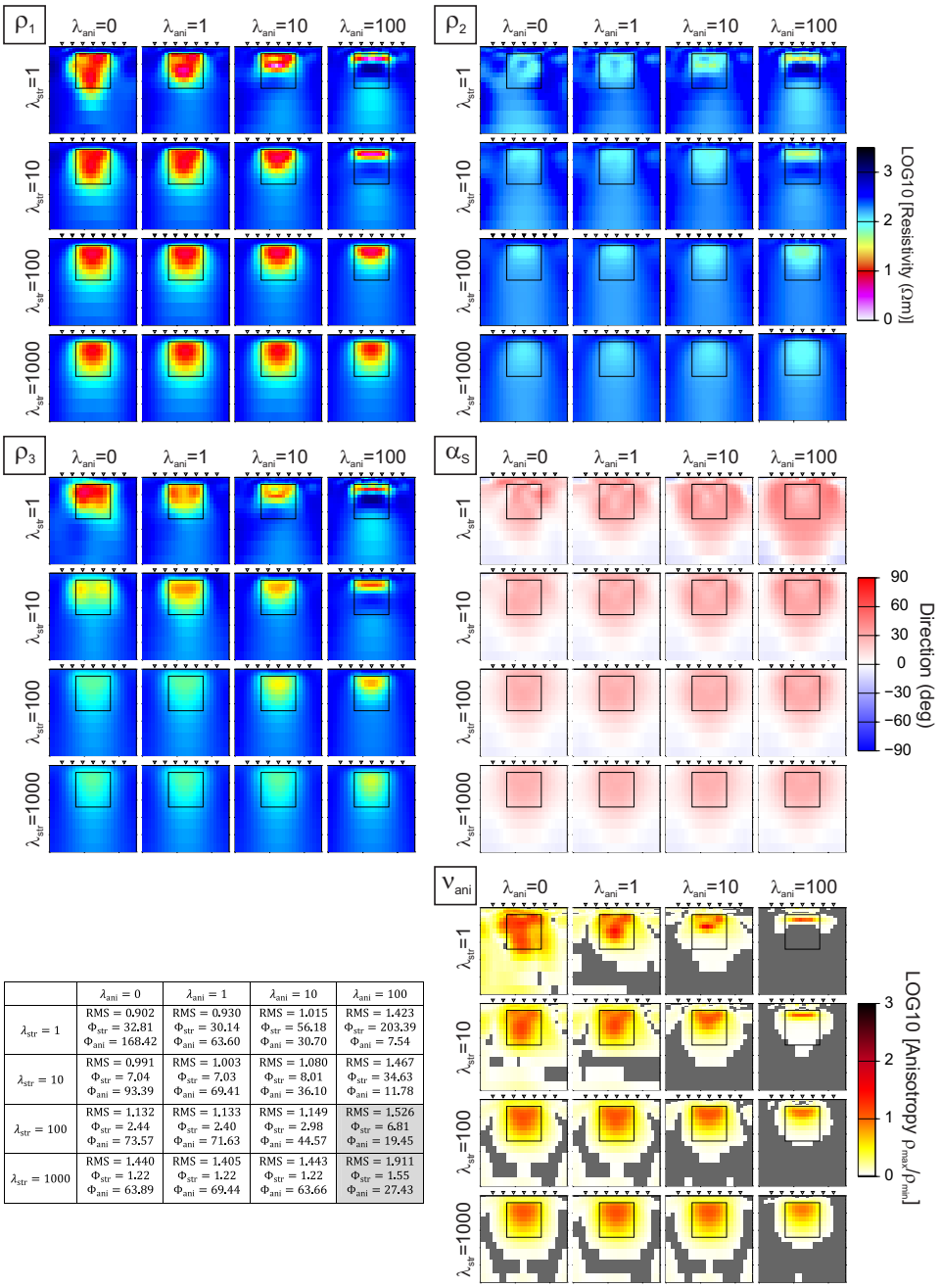

	$\lambda_{ani} = 0$	$\lambda_{ani} = 1$	$\lambda_{ani} = 10$	$\lambda_{ani} = 100$
$\lambda_{str} = 1$	RMS = 0.902 Φ_{str} = 32.81 Φ_{ani} = 168.42	RMS = 0.930 Φ_{str} = 30.14 Φ_{ani} = 63.60	RMS = 1.015 Φ_{str} = 56.18 Φ_{ani} = 30.70	RMS = 1.423 Φ_{str} = 203.39 Φ_{ani} = 7.54
$\lambda_{str} = 10$	RMS = 0.991 Φ_{str} = 7.04 Φ_{ani} = 93.39	RMS = 1.003 Φ_{str} = 7.03 Φ_{ani} = 69.41	RMS = 1.080 Φ_{str} = 8.01 Φ_{ani} = 36.10	RMS = 1.467 Φ_{str} = 34.63 Φ_{ani} = 11.78
$\lambda_{str} = 100$	RMS = 1.132 Φ_{str} = 2.44 Φ_{ani} = 73.57	RMS = 1.133 Φ_{str} = 2.40 Φ_{ani} = 71.63	RMS = 1.149 Φ_{str} = 2.98 Φ_{ani} = 44.57	RMS = 1.526 Φ_{str} = 6.81 Φ_{ani} = 19.45
$\lambda_{str} = 1000$	RMS = 1.440 Φ_{str} = 1.22 Φ_{ani} = 63.89	RMS = 1.405 Φ_{str} = 1.22 Φ_{ani} = 69.44	RMS = 1.443 Φ_{str} = 1.22 Φ_{ani} = 63.66	RMS = 1.911 Φ_{str} = 1.55 Φ_{ani} = 27.43

Figure 4: 2-D anisotropic inversion of noisy synthetic data generated by a model with a square anisotropic box ($\varrho_1 = \varrho_3 = 10$ Ωm, $\varrho_2 = 10$ Ωm, $\alpha_S = 30°$) embedded in a homogeneous halfspace ($\varrho_{\text{host}} = 300$ Ωm) for different structure and anisotropy penalty weights. For detailed description of the model sections, see caption to Fig. 3. The table in the bottom left panel summarizes the structure and anisotropy penalties of the resulting models as well as their RMS's. Models with RMS > 1.5 are grayed.

3.1.3 Isotropic Anomaly

Another important test consists in checking any spurious anisotropy produced by the anisotropic inversion if data due to an isotropic structure are inverted. We consider the same 2-D box model as above but

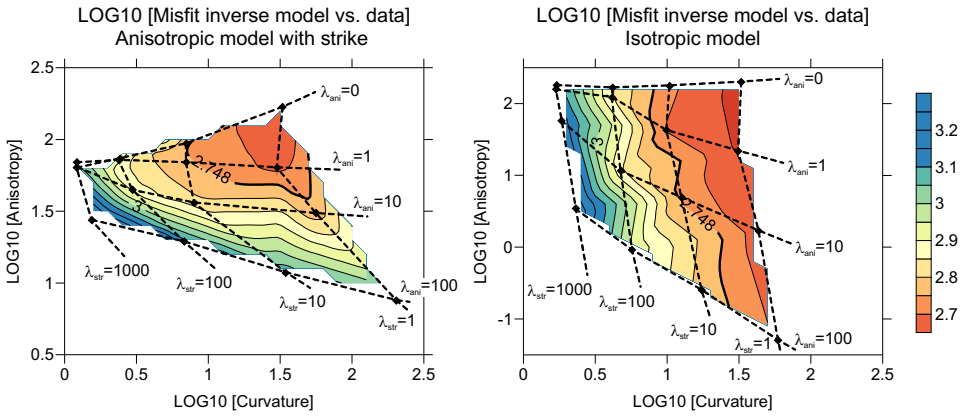

Figure 5: Regularization L-surfaces for the inversion of an anisotropic box data (left plot) and for its isotropic version (right). The dashed lines connect model points with the same structure and anisotropy penalty weights. The bold isoline marks a misfit contour of 760 which corresponds to the RMS = 1.000.

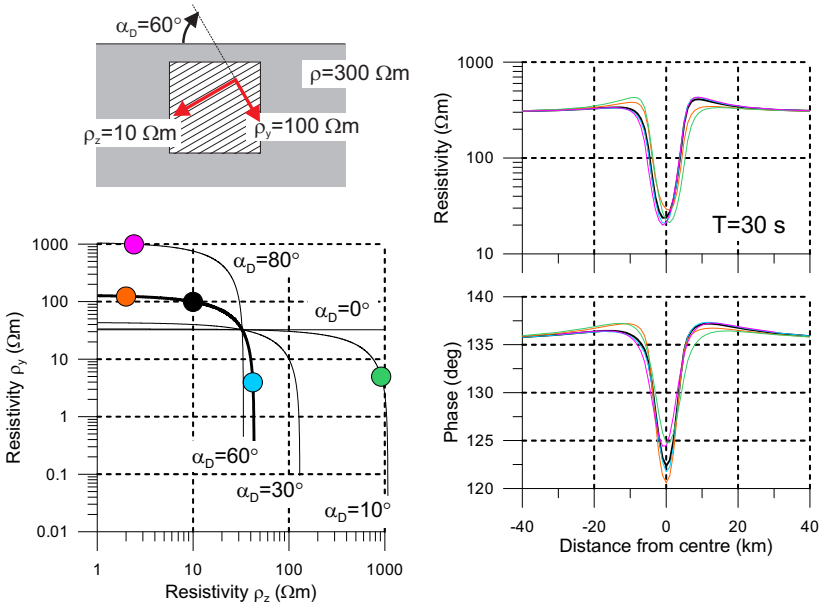

Figure 6: 2-D box model with dipping anisotropy (top left panel) and MT apparent resistivity and phase curves for a series of models with various principal resistivities ϱ_y, ϱ_z and anisotropy dips α_D which would be exactly equivalent in 1-D case (right panels). The bottom left panel shows lines of pairs of the resistivities ϱ_y, ϱ_z which are equivalent for indicated dips α_D in 1-D case. The colored circles correspond to anisotropy parameters which produced the 2-D MT curves in the right panels.

with an isotropic anomaly with $\varrho_{\text{iso}} = 10$ Ωm. The top panel in Fig. 8 shows models provided by a standard isotropic inversion for several structure penalty weights. The same inversion runs were then carried out for three principal resistivities aligned with the model coordinate frame. The anisotropy angles were omitted here since no reason existed to include them for data which did not contain any significant diagonal impedance elements. Results of the anisotropic inversion are displayed in the bottom panel of Fig. 8. Clearly a superior result is obtained with $\lambda_s = 100$ and $\lambda_a = 10$, though the data are

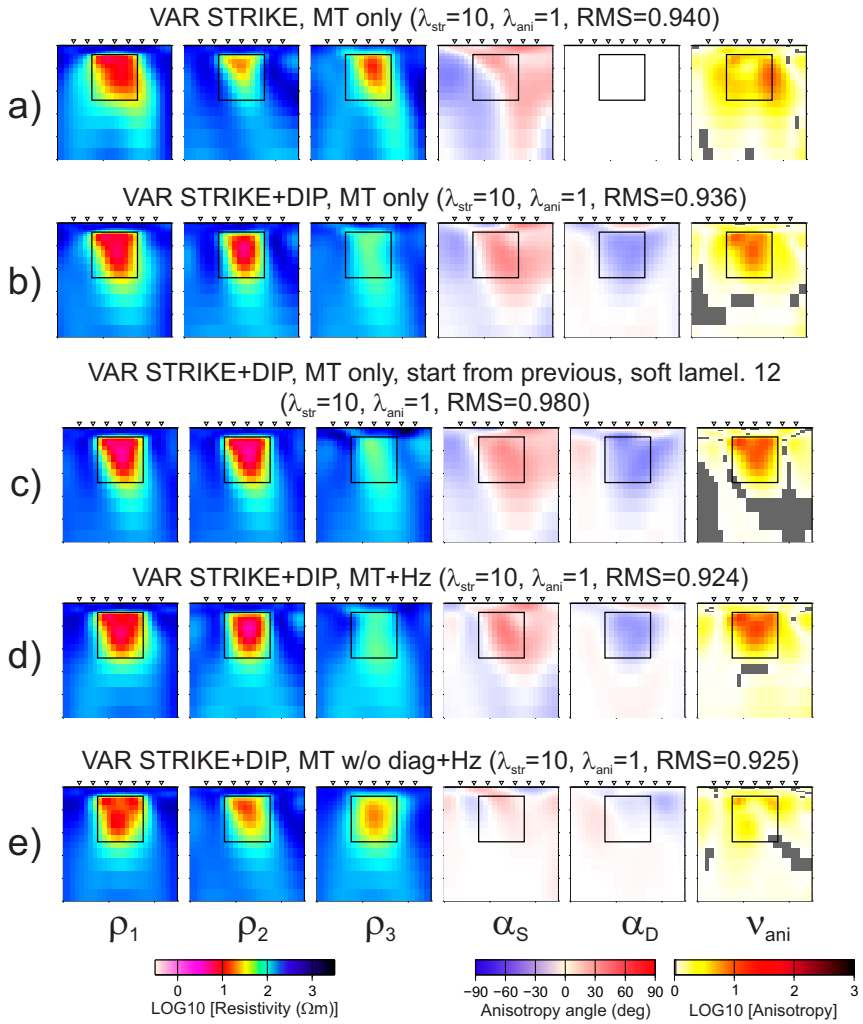

Figure 7: 2-D anisotropic inversion of synthetic MT data generated by the model with dipping anisotropy from Fig. 6. a) Inversion of MT impedances for three principal resistivities and anisotropy strike; dip is fixed at $\alpha_D = 0°$. b) Inversion of MT impedances for three principal resistivities and anisotropy strike and dip. c) The same as b) but with a soft constraint applied to minimize the difference between the resistivities ϱ_1 and ϱ_2 (forced lamelarity of anisotropic domains). d) The same as b) but the inverted data set was extended by vertical geomagnetic transfer functions (induction arrows). e) The same as d) with diagonal impedances left out from the inverted data set.

slightly underfitted in this case (RMS = 1.130). With smaller structure and zero anisotropy penalties, we observe both considerable spurious anisotropy as well as structural instability. For large penalties, new spurious anisotropy may appear due to the fact that the yx MT curves (H-mode) can be fitted satisfactorily with less conductivity (i.e., with less structure) than the xy (E-mode) curves. The vertical resistivity, ϱ_3, evidently gives the most variable images due to the low sensitivity of the MT fields with respect to this paramter.

The L-surface for this synthetic test is shown in the right-hand side panel in Fig. 5. The shape of this surface is slightly different from that for the anisotropic case studied earlier. As we cannot worsen the model complexity and data misfit by strengthening the anisotropy penalty applied to isotropic data, the L-surface does not show a target increase for large anisotropy penalties as it is the case for anisotropic data.

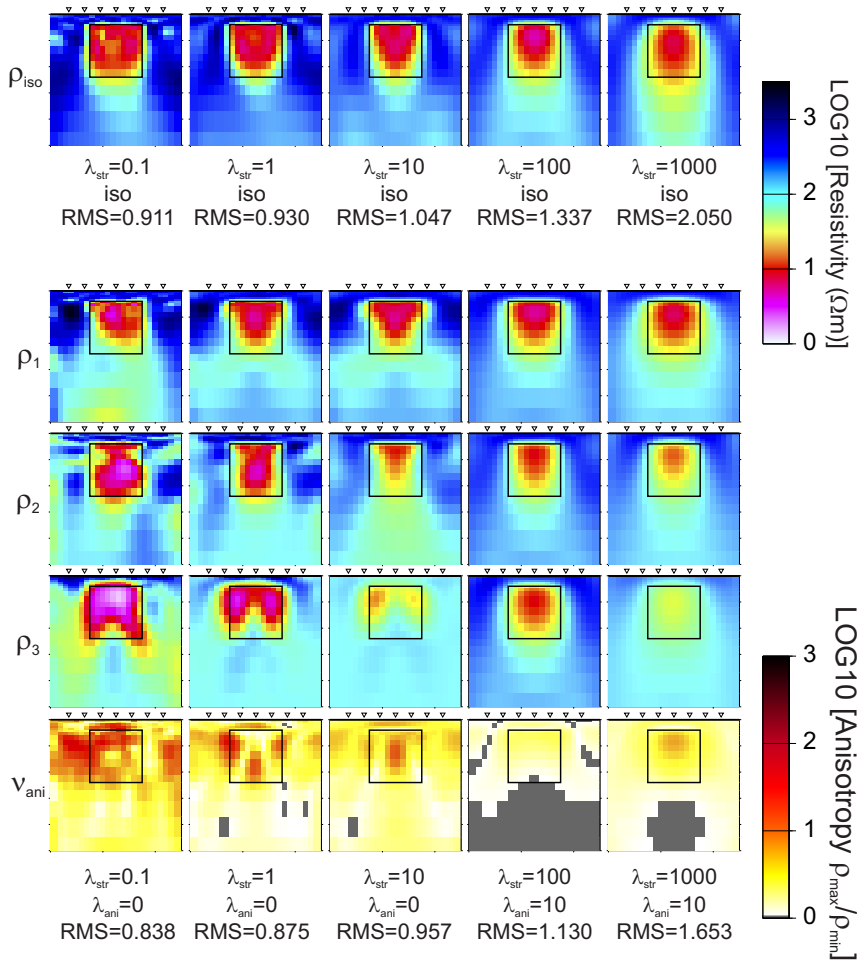

Figure 8: Top: Isotropic inversion for isotropic conductivity in a square box anomaly for several structural penalties. Bottom: Anisotropic inversion for three principal resistivities aligned with the model coordinate frame for the same data as above for several pairs of structure and anisotropy penalties.

3.2 Near-Surface Anisotropic Distorter above a Discordant Anisotropic Layer

A special class of anisotropic models are structures with highly anisotropic, near-surface bodies which act as strong MT distorters by virtue of chanelling the telluric currents in a direction generally oblique with respect to the structural strike. Such distortions may even result in MT phases rolling out of their natural quadrant (Pek, 2009), and may be a source of convergency difficulties for the NLCG inversion procedure. Here we only briefly visit a synthetic test for MT data generated by a model consisting of a near-surface, highly anisotropic block ($\varrho_1 = \varrho_3 = 1$ Ωm, $\varrho_2 = 100$ Ωm, $\alpha_s = 20°$) in the uppermost crust underlain by a mid- to lower-crustal layer with increasing anisotropy from the left to the right and discordant anisotropy strike, $\alpha_S = -20°$. Complete parameters of the model are shown in the bottom right panel in Fig. 9. The model produces the out-of-quadrant phases but only for rotated data, not in the model coordinate frame.

The inversion was run for all three principal resistivities and for the anisotropy strike. The size of the inverse problem was: 950 model cells, 3800 model parameters, 1440 data items. Results of the inversion are shown in Fig. 9 for the regularization weights $\lambda_s = 10$, $\lambda_a = 3$. RMS of the final model is 1.060. The inverse model captures the true structure satisfactorily, especially parameters of the near surface distoring body. The resistive part of the deep layer to the left is shifted towards the surface but its anisotropy to the right is recovered well both as to the size and geometrical position. The part of the layer immediately

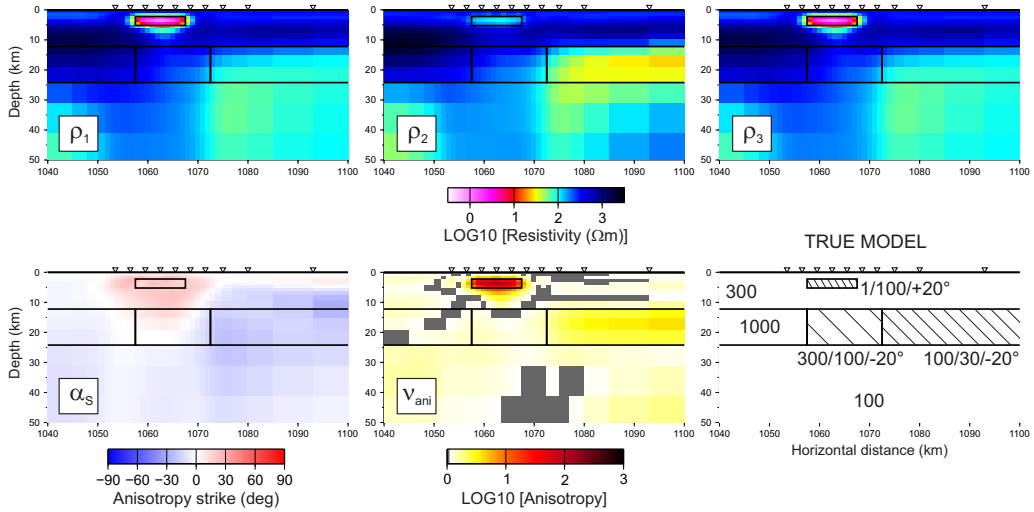

Figure 9: Inversion of noisy synthetic MT data generated by a model of a shallow, strongly anisotropic anomaly and a layer of moderate anisotropy increasing from the left to the right beneath the anomalous block. The panels show the principal resistivities (ϱ_1, ϱ_2, ϱ_3, top panels), anisotropy strike and anisotropy ratio (α_S, ν_{ani}, bottom panels) recovered by the inversion. The bottom rightmost panel shows the geometry and parameters of the data generating (true) model, resistivities are given in Ωm. The regularization weights used are $\lambda_s = 10$, $\lambda_a = 3$. The inverse model's RMS is 1.060.

beneath the distorter is not sensed properly, which could be expected.

This model test presents an exercise with a more complex anisotropic structure, which could be recovered sufficiently well by the NLCG inverse procedure. For this kind of models with mixed anisotropy strikes one open question still remains, specifically that of misdetermined structural strikes for the 2-D modeling.

4 Field Data: MT Data from Southern Portugal

In our previous paper on the 1-D MT inversion for anisotropic media, we tested the developed method on practical data from southern Portugal, from the transition of two southernmost prominent zones of the Iberian Variscides, the Southern Portuguese Zone (SPZ) and the Ossa Morena Zone (OMZ) (Pek and Santos, 2006). A long and narrow belt of mafic and ultramafic rocks lines up at the border between these zones. Those rocks are currently interpreted as an ophiolite complex (Badajoz Acebuches Ophiolite Complex, BAOC). In the Portuguese mainland the BAOC represents the southern border of the Beja Igneous Complex (BIC) deformed in the vicinity of the Ferreira-Ficalho thrust (Figueiras *et al.*, 2002). Without further repeating the geological background of the area, detailed in (Pek and Santos, 2006), it has been concluded that the geological context of the study area is greatly favourable to the presence of anisotropic structures at upper to middle crust depths. References to the presence of anisotropic black schists in south Iberia, as well as to the anisotropic behaviour of MT data can be found in (Pous *et al.*, 2004).

Pek and Santos (2006) modeled a small subset of data from a large-scale broad-band MT experiment in southern Portugal (Almeida *et al.*, 2001) which crosses the contact area between the SPZ and OMZ. They used a 1-D inversion procedure for anisotropic structures and 2-D trial-and-error forward modeling to fit the MT impedances. Though excellent fit was achieved earlier by 2-D inverting the principal MT curves, some specific features in the data suggested that non-negligible non-2-D effects influence the MT field, especially those related to the diagonal impedance elements (Pek and Santos, 2006). Anisotropy was adopted as a possible mechanism for explaining the non-2-D features in the data, though other reasons cannot be excluded either, particularly static distortions or off-profile 3-D effects.

Without attempting any deeper interpretation of the above MT data, we only want to demonstrate here how the trial-and-error modeling by Pak and Santos (2006) compares with results of the 2-D anisotropic

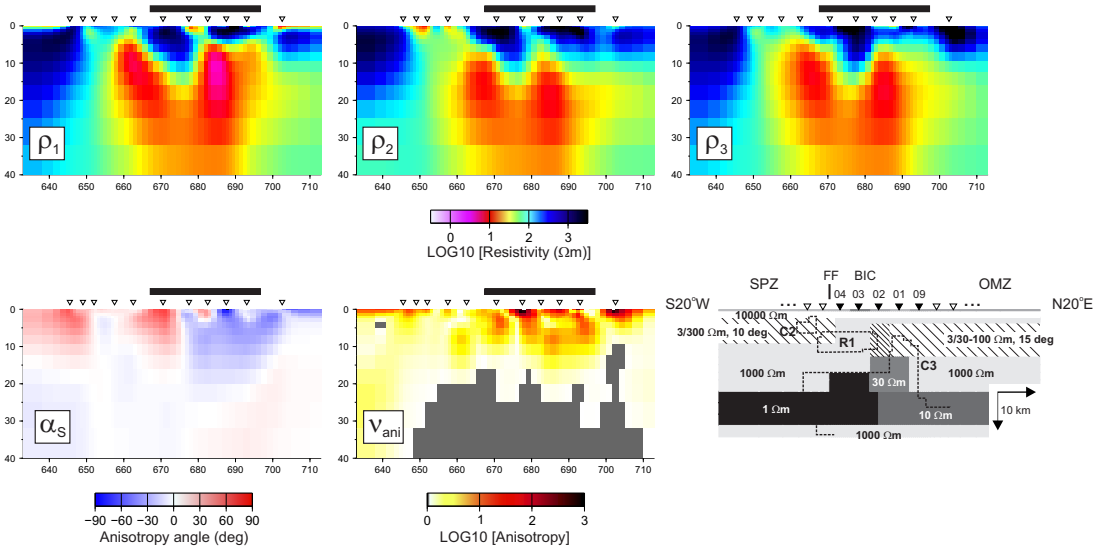

Figure 10: Inverse 2-D anisotropic model from a subset of MT data across the contact area between the SPZ and OMZ, southern Portugal. The model was obtained with regulariztion penalty weights $\lambda_s = 300$, $\lambda_a = 100$. The size of the model was: 1701 model cells, 8505 model parameters, 792 data items. The bottom right panel repeats the model obtained by a combined 1-D anisotropic inversion and 2-D trial-and-error forward modeling by Pek and Santos (2006). The black lines above the plots indicate the section of the profile which was modeled in the paper by Pek and Santos (2006) (sites 04, 03, 02, 01, 09 in the original model). See the text for the acronyms.

inversion of the same data subset. We present one of the inverse anisotropic models in Fig. 10. All three principal resistivities, anisotropy strike and dip were inverted in this case. A significant dip was detected only in the conductive channel between two resistors in the central part of the profile which may indicate vertical current channeling in this zone. In other domains of the model, the dip is featureless, and therefore is not displayed in Fig. 10.

The interpreted principal resistivities in Fig. 10 are very similar to each other, and we would rather conclude that the underlying structure is isotropic. The main structures revealed by the inversion do coincide well with the results of the isotropic inversion by Almeida *et al.* (2001), which are indicated in the bottom left model in Fig. 10 by dashed contours labeled C2, R1, C3. Only the localized conductor C2 by Almeida *et al.* (2001) is substantially larger in our model and interconnected with deep crustal conductors. This can be explained by the structure being oversmoothed due to large structural penalty imposed ($\lambda_s = 300$). In fact, this conductor becomes more focused if the structure penalty is relaxed, but for the price of unrealistically increased anisotropy in other parts of the model.

Effect of the anisotropy in the model is mainly seen in improved fit to the secondary, diagonal impedances, which are non-symmetric ($Z_{xx} + Z_{yy} \neq 0$) and cannot be thus explained in terms of a purely 2-D model. Similarly as in the trial-and-error result, the anisotropy is practically completely concentrated in the first 10 km layer of the model. A strong anisotropic feature is observed beneath the BIC and seems to represent a sub-vertical current channel because of $\varrho_1 \approx \varrho_2 \ll \varrho_3$ and a large dip in this zone. The originally strongly anisotropic continuous layer modeled beneath the SPZ in the SW of the profile is not necessarily supported by the new 2-D model, and may occur due to a strong effect of the conductor C2. The moderately anisotropic layer beneath the OMZ in the NE part of the profile does appear in the inverse model in the basement of the continuous crustal resistor. The anisotropy strike in this layer is, however, of opposite sign in comparison with the original model. Some of the very shallow anisotropy is likely to be due to static distortions in the MT curves which could not be removed completely, especially from the diagonal impedances. Interference of the static shifts with anisotropy is one of the questions still open to further investigations.

5 Conclusion

We presented an algorithm for the 2-D inversion of magnetotelluric data for conductivity distributions with arbitrary anisotropy. The inversion is based on a Polak-Ribière version of the NLCG algorithm with a simple Jacobi pre-conditioning, and is the same procedure as Rodi and Mackie's (2001) technique used for isotropic inversion. We tried to show all the algorithmic issues of the anisotropic inversion and demonstrate all of them working together. Though the synthetic tests carried out in this contribution were only very simple, they could demonstrate basic features of the anisotropic inversion as well as an overview of ambiguities and quasi-equivalencies that may appear at interpreting anisotropic models. Though the most significant ambiguity issues known from 1-D magnetotellurics (sensitivity w.r.t. the vertical conductivity, ambiguities for dipping anisotropies) cannot be theoretically justified in 2-D structures, they are manifested in practice by poor resolution and by quasi-equivalencies of certain model parameters in 2-D anisotropic sections. This situation as well as missing theoretical results cause that a lot more weight is put on numerical experiments and tests in 2-D MT situations.

As regards the outputs of the synthetic tests, we could arrive at following conclusions: (i) similarly as in the 1-D case, the most reliable inversion results are obtained for structures with azimuthal anisotropy, (ii) vertical resistivity is almost indistinguishable in 2-D models though it cannot be omitted completely because of its irreplaceable role in the forward modeling step; forcing lamelar or tubular anisotropy may be a baypass for coping with the unresolved vertical conductivity, (iii) similarly as in 1-D MT case, anisotropy dip is an unresolvable parameter unless additional structural information is available; effect of the true dip increases if anisotropy strike increases (i.e., if lamelas dip in the direction close to the structural strike); if false dip is fixed in the inverse procedure in such a case, the recovered anisotropy strike may be not correct, (iv) care must be taken if resistivities from dipping structures are interpreted; the resistivities may be not correct due to the action of the structure/anisotropy penalties.

With regard to practical data, we could arrive to a satisfactory fit of the experimental data in a few cases. Nevertheless, verifying the models cannot be based on the MT fit alone, and will require additional support from other geodata. Moreover, a number of more or less algorithmic questions remains still open, e.g., (i) how much do static distortions and 3-D off-profile effects in MT data interfere with 2-D anisotropic interpretations, (ii) how much significant is a correct determination of the 2-D structural strike for the 2-D anisotropic inversion if varying or mixed anisotropy strikes mask the true structural axis of homogeneity, (iii) how oblique anisotropies are interpreted by the 2-D inversion, especially those producing out-of-quadrant anomalous MT phases.

Acknowledgements

Financial support of the Czech Sci. Found. to this work, under contract No. P210-10-2227, is highly acknowledged.

References

Almeida, E., Pous, J., Monteiro Santos, F., Fonseca, P., Marcuello, A., Queralt, P., Nolasco, R., and Mendes-Victor, L.: Electromagnetic imaging of a transpressional tectonics in SW Iberia. *Geophys. Res. Lett.*, **28** (2001), 439–442.

Andrei, N.: 40 conjugate gradient algorithms for unconstrained optimization. A survey on their definition. *ICI Technical Report* No. 13/08, March 14, 2008.

Bahr, K., and Simpson, F.: Electrical anisotropy below slow- and fast-moving plates: Paleoflow in the upper mantle? *Science*, **295** (2002), 1270–1272.

Bertsekas, D. P., and Bertsekas, D. P.: *Nonlinear Programing*. Athena Scientific, 2nd edition, 1999, 794 pp.

Brasse, H., Kapinos, G., Li, Y., Mütschard, L., Soyer, W., and Eydam, D.: Structural electrical anisotropy in the crust at the South-Central Chilean continental margin as inferred from geomagnetic transfer functions. *Phys. Earth Planet. Inter.*, **173** (2009), doi:10.1016/j.pepi.2008.10.017.

Constable, S. C., Parker, R. L., and Constable, C. G.: Occam's inversion: a practical algorithm for generating smooth models from EM sounding data. *Geophysics*, **52** (1987), 289–300.

Červ, V., and Pek, J.: Numerical solution of the two-dimensional geomagnetic induction problem. *Studia geoph. et geod.* (1981), **25**, 69–80.

Davydycheva, S., Druskin, V., and Habashy, T.: An efficient finite-difference scheme for electromagnetic logging in 3D anisotropic inhomogeneous media. *Geophysics*, **68** (2003), 1525–1536.

deGroot-Hedlin, C., and Constable, S. C.: Occam's inversion to generate smooth, two-dimensional models from magnetotelluric data. *Geophysics*, **55** (1990), 1613–1624.

Eisel, M., and Haak, V.: Macro-anisotropy of the electrical conductivity of the crust: A magnetotelluric study from the German Continental Deep Drilling site (KTB). *Geophys. J. Int.*, **136** (1999), 109–122.

Eisel, M., Haak, V., Pek, J., and Červ, V.: A magnetotelluric profile across the German Deep Drilling Project (KTB) area: Two- and three-dimensional modeling results. *J. Geophys. Res.*, **106** [B8] (2001), 16061–16073.

Figueiras, J., Mateus, A., Gonalves, M.A., Waerenbourgh, J., and Fonseca, P.: Geodynamic evolution of the South Variscan Iberian Suture as recorded by mineral transformations. *Geodinamica Acta*, **15** (2002), 45–61.

Hamilton, M. P., Jones, A. G., Evans, R. L., Evans, S., Fourie, C. J. S., Garcia, X., Mountford, A., Spratt, J. E., and the SAMTEX Team: Electrical anisotropy of South African lithosphere compared with seismic anisotropy from shear-wave splitting analyses. *Phys. Earth Planet. Inter.*, **158** (2006), 226–239.

Heise, W., and Pous, J.: Anomalous phases exceeding 90° in magnetotellurics: Anisotropic model studies and a field example. *Geophys. J. Int.*, **155** (2003), 308–318.

Hou, J., Mallan, R. K., and Torres-Verdn, C.: Finite-difference simulation of borehole EM measurements in 3D anisotropic media using coupled scalar-vector potentials. *Geophysics*, **71** (2006), G225–G233.

Jupp, D. L. B., and Vozoff, K.: Two-dimensional magnetotelluric inversion. *Geophys. J. Roy. Astr. Soc.*, **50** (1977), 333–352.

Lezaeta, P., and Haak, V.: Beyond magnetotelluric decomposition: Induction, current channeling, and magnetotelluric phases over 90 degrees. *J. Geophys. Res.–SE*, **108** (2003), Art. No. 2305.

Li, Y.: A finite-element algorithm for electromagnetic induction in two-dimensional anisotropic conductivity structures. *Geophys. J. Int.*, **148** (2002), 389–401.

Li, Y., Pek, J., and Brasse, H.: Magnetotelluric inversion for 2D anisotropic conductivity structures. In Hoerdt, A., and Stoll, J. B., Eds., *Proceed. 20th Colloq. "Electromagnetic Depth Investigations"*, Königstein, 29. 9.–3. 10. 2003, DGG, pp. 250–259.

Li, Y., and Pek, J.: Adaptive finite element modelling of two-dimensional magnetotelluric fields in general anisotropic media. *Geophys. J. Int.*, **175** (2008), 942–954.

Mareschal, M., Kellett, R. L., Kurtz, R. D., Ludden, J. N., Ji, S., and Bailey, R. C.: Archean cratonic roots, mantle shear zones and deep electrical anisotropy. *Nature*, **375** (1995), 134–137.

Newman, G. A., and Alumbaugh, D. L.: Three-dimensional magnetotelluric inversion using non-linear conjugate gradients. *Geophys. J. Int.*, **140** (2000), 410–424.

Newman, G. A., and Boggs, P. T.: Solution accelerators for large-scale three-dimensional electromagnetic inverse problems. *Inverse Problems*, **20** (2004), S151–S170.

Padilha, A. L., Vitorello, I., Pádua, M. B., and Bologna, M. S.: Lithospheric and sublithospheric anisotropy beneath central-southeastern Brazil constrained by long period magnetotelluric data. *Phys. Earth Planet. Inter.*, **158** (2006). 190-209.

Pain, C., Herwanger, J. V., Saunders, J. H., Worthington, M. H., and Oliveora, C. R. E.: Anisotropic resistivity inversion. *Inverse Problems*, **19**, 1081–1111.

Pek J., and Verner, T.: Finite-difference modelling of magnetotelluric fields in two-dimensional anisotropic media. *Geophys. J. Int.*, **128** (1997), 505–521.

Pek, J., and Santos, F. A. M.: Magnetotelluric impedances and parametric sensitivites for 1-D generally anisotropic layered media. *Computers & Geosciences*, **28** (2002), 939–950.

Pek, J., Santos, F. A. M., and Li, Y.: Parametric sensitivities for 2-D anisotropic magnetotelluric model.

In Hoerdt, A., and Stoll, J. B., Eds., *Proceed. 20th Colloq. "Electromagnetic Depth Investigations"*, Königstein, 29. 9.–3. 10. 2003, DGG, pp. 240–249.

Pek, J., and Santos, F. A. M.: Magnetotelluric inversion for anisotropic conductivities in layered media. *Phys. Earth Planet. Inter.*, **158** (2006), 139–158.

Pek, J.: Effects of electrical anisotropy on magnetotelluric data: modelling and experiments. In *Modern methods of electromagnetic data measurement, processing and interpretation* (pp. 110–135), V. V. Spichak (Ed.), LIBROKOM Publ., Moscow 2009, 304 pp. (in Russian).

Pous, J., Munoz, G., Heise, W., Melgarejo, J.C., and Quesada, C.: Electromagnetic imaging of Variscan crustal structures in SW Iberia: the role of interconneted graphite. *Earth Planet. Sci. Lett.*, **217** (2004), 435–450.

Press, W. H., Flannery, B. P., Teukolsky, S. A., and Vetterling, W. T.: *Numerical recipes: the art of scientific computing*. Cambridge University Press, NY, USA, 1986.

Ramananjaona, C., and MacGregor, L.: 2.5D inversion of CSEM data in a vertically anisotropic earth. *J. Phys.: Conf. Ser.*, **255** (2010), doi:10.1088/1742-6596/255/1/012004.

Reddy, I. K., and Rankin, D.: Magnetotelluric response of laterally inhomogeneous and anisotropic media. *Geophysics*, **40** (1975), 1035–1045.

Rodi, W. L.: A technique for improving the accuracy of finite element solutions for magnetotelluric data. *Geophys. J. Roy. Astr. Soc.*, **44** (1976), 483-506.

Rodi, W., and Mackie, R. L.: Nonlinear conjugate gradients algorithm for 2-D magnetotelluric inversion. *Geophysics*, **66** (2001), DOI:10.1190/1.1444893.

Roux, E., Moorkamp, M., Jones, A. G., Bischoff, M., Endrun, B., Lebedev, S., and Meier, T.: Joint inversion of long-period magnetotelluric data and surface-wave dispersion curves for anisotropic structure: Application to data from Central Germany. *Geophys. Res. Lett.*, doi:10.1029/2010GL046358

Ruiz-Constán, A., Galindo-Zaldivar, J., Pedrera, A., Arzate, J. A., Pous, J., Anahnah, F., Heise, W., Monteiro Santos, F. A., and Marín-Lechado, C.: Deep deformation pattern from electrical anisotropy in an arched orogen (Betic Cordillera, western Mediterranean). *Geology*, **38** (2010), 731–734.

Simpson, F.: Resistance to mantle flow inferred from the electromagnetic strike of the Australian upper mantle. *Nature*, **412** (2001), 632–635.

Tikhonov, A. N., and Arsenin, V. Y.: *Solution of ill-posed problems*. Winston and Sons, 1977, 285 pp.

Wang, T., and Fang, S.: 3-D electromagnetic anisotropy modeling using finite differences. *Geophysics*, **66** (2001), 1386–1398.

Wannamaker, P. E.: Anisotropy versus heterogeneity in continental solid earth electromagnetic studies: fundamental response characteristics and implications for physicochemical state. *Surv. Geophys.*, **26** (2005), 733-765.

Weaver, J. T., Le Quang, V. B., and Fischer, G.: A comparison of analytical and numerical results for a two-dimensional control model in electromagnetic induction - I. B-polarization calculations. *Geophys. J. R. astr. Soc.*, **82** (1985), 263–278.

Weaver, J. T., Le Quang, V. B., and Fischer, G.:, 1986. A comparison of analytical and numerical results for a 2 D control model in electromagnetic induction - II. E-polarization calculations. *Geophys. J. R. astr. Soc.*, **87** (1986), 917–948.

Weckmann, U., Ritter, O., and Haak, V.: A magnetotelluric study of the Damara Belt in Namibia. 2. MT phases over 90 degrees reveal the internal structure of the Waterberg Fault/Omaruru Lineament. *Phys. Earth Planet. Inter.*, **138** (2003), 91–112.

Weidelt, P.: 3-D conductivity models: Implications of electrical anisotropy. In Oristaglio, M., and B. Spies, Eds., *Three-dimensional electromagnetics*, Geophys. Dev. Series, 7, Soc. Explor. Geophys., Tulsa, OK, 119–137, 1999.

Weiss, C. J., and Newman, G. A.: Electromagnetic induction in a fully 3-D anisotropic earth. *Geophysics*, **67** (2002), 1104–1114.

Zaslavsky, M., Druskin, V., Davydycheva, S., Knizhnerman, L., Abubakar, A., and Habashy, T.: Hybrid finite-difference integral equation solver for 3D frequency domain anisotropic electromagnetic problems. *Geophysics*, **76** F123 (2011), DOI:10.1190/1.3552595.